JACS
JOURNAL OF THE AMERICAN CHEMICAL SOCIETY
Article
Cite This: J. Am. Chem. Soc. 2019, 141, 19839−19849
pubs.acs.org/JACS

Stable Ultraconcentrated and Ultradilute Colloids of $CsPbX_3$ (X = Cl, Br) Nanocrystals Using Natural Lecithin as a Capping Ligand

Franziska Krieg,[†,‡] Quy K. Ong,[§] Max Burian,[∥] Gabriele Rainò,[†,‡] Denys Naumenko,[⊥] Heinz Amenitsch,[⊥] Adrian Süess,[†,‡] Matthias J. Grotevent,[†,#] Frank Krumeich,[†] Maryna I. Bodnarchuk,[†,‡] Ivan Shorubalko,[#] Francesco Stellacci,[§] and Maksym V. Kovalenko*[,†,‡]

[†]Institute of Inorganic Chemistry, Department of Chemistry and Applied Bioscience, ETH Zürich, Vladimir Prelog Weg 1, CH-8093 Zürich, Switzerland

[‡]Laboratory for Thin Films and Photovoltaics and [#]Laboratory for Transport at Nanoscale Interfaces, Empa−Swiss Federal Laboratories for Materials Science and Technology, Überlandstrasse 129, CH-8600 Dübendorf, Switzerland

[§]Institute of Materials, École Polytechnique Fédérale de Lausanne (EPFL), Lausanne, Switzerland

[∥]Swiss Light Source, Paul Scherrer Institut, 5232 Villigen PSI, Switzerland

[⊥]Institute of Inorganic Chemistry, Graz University of Technology, Stremayrgasse 9/V, 8010 Graz, Austria

Supporting Information

ABSTRACT: Attaining thermodynamic stability of colloids in a broad range of concentrations has long been a major thrust in the field of colloidal ligand-capped semiconductor nanocrystals (NCs). This challenge is particularly pressing for the novel NCs of cesium lead halide perovskites ($CsPbX_3$; X = Cl, Br) owing to their highly dynamic and labile surfaces. Herein, we demonstrate that soy lecithin, a mass-produced natural phospholipid, serves as a tightly binding surface-capping ligand suited for a high-reaction yield synthesis of $CsPbX_3$ NCs (6−10 nm) and allowing for long-term retention of the colloidal and structural integrity of $CsPbX_3$ NCs in a broad range of concentrations—from a few ng/mL to >400 mg/mL (inorganic core mass). The high colloidal stability achieved with this long-chain zwitterionic ligand can be rationalized with the Alexander−De Gennes model that considers the increased particle−particle repulsion due to branched chains and ligand polydispersity. The versatility and immense practical utility of such colloids is showcased by the single NC spectroscopy on ultradilute samples and, conversely, by obtaining micrometer-thick, optically homogeneous dense NC films in a single spin-coating step from ultraconcentrated colloids.

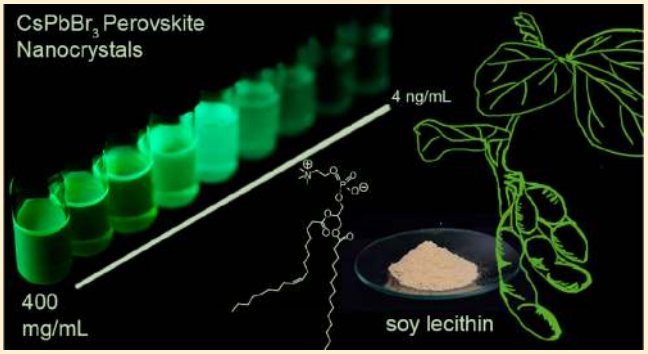

INTRODUCTION

Colloidal nanocrystals (NCs) of lead halide perovskites ($APbX_3$; A = Cs, formamidinium; X = Cl, Br, I) are new semiconductor NCs which have both unique optical characteristics as well as specific challenges.[1] Defect-tolerant photophysics,[2] outstanding photoluminescence (PL) characteristics, narrow emitting bands, high quantum yields (QYs), spectral tunability, and facile synthesis make perovskite NCs appealing classical light sources (in LCD and LED displays,[3] lasers,[4] optical communication,[5] scintillators[6]) as well as single-photon sources.[7] Conversely, perovskite NCs are also pursued as promising light harvesters for solar cells[8] and photodetectors.[5a,9]

The surface state of semiconductor NCs has been the dominant factor defining the optical and electronic characteristics of individual NCs and their assemblies.[10] The inorganic (NC core)−organic (ligands, solvents) interface is quintessential for the entire life cycle of a semiconductor NC—from its nucleation and growth to integration into devices.[11] The surface chemistry of perovskite NCs has been shown to be vastly different from conventional semiconductor NCs, chiefly due to their ionic bonding and low lattice energy within the lead halide NC core (structural lability) and at the inorganic−organic interface.[12] Most specific challenges are the susceptibility of the NC cores to water and many other solvents due to their finite solubility and the loose binding of the surface-capping ligands.[13] These have been the major obstacles for studying, processing, and applications of perovskite NCs. For instance, rapid ligand desorption renders colloids unstable and eventually causes morphological degradation and coalescence of these NCs. Unsurprisingly, a rapid surge of reports is targeting these difficulties by the judicious choice of the solvents, ligands, and other additives for the synthesis and isolation protocols.[11l,n,12c,d,14] Alternatively, NC films can be subjected to various surface stabilization and matrix-encapsulation strategies.[7j,16]

Received: September 18, 2019
Published: November 25, 2019

DOI: 10.1021/jacs.9b09969
J. Am. Chem. Soc. 2019, 141, 19839−19849

The ideal ligand system is allowing for efficient synthesis and subsequent processing. Common solution-processing techniques—spin coating, inkjet printing, doctor blading, slot die coating, or screen printing—all require concentrated and stable colloids. Obtaining thick, optically homogeneous, and dense films of $CsPbBr_3$ and $FAPbBr_3$ NCs with high PL QYs is of paramount importance in quantum dot-color filter displays,[3a,i,17] wherein the emissive layer must be several micrometers thick in order to completely absorb the blue backlight to reach optimal luminance and a wide color gamut. On the other hand, highly dilute NC systems are required for engineering quantum light sources.[7]

In this study, we sought to devise an effective ligand system that allows retention of the colloidal state, structural integrity, and optical characteristics over a broad range of $CsPbBr_3$ NC concentrations. Using natural soy lecithin as a capping ligand (Figure 1a and 1b), we obtained concentrations of $CsPbX_3$ NCs exceeding 400 mg/mL (inorganic core mass/total volume of the colloid), i.e., approximately 30% by volume (Figure 1c). Furthermore, tight ligand binding allows attaining the colloidal state and maintaining NC integrity in a broad concentration range down to few ng/mL.

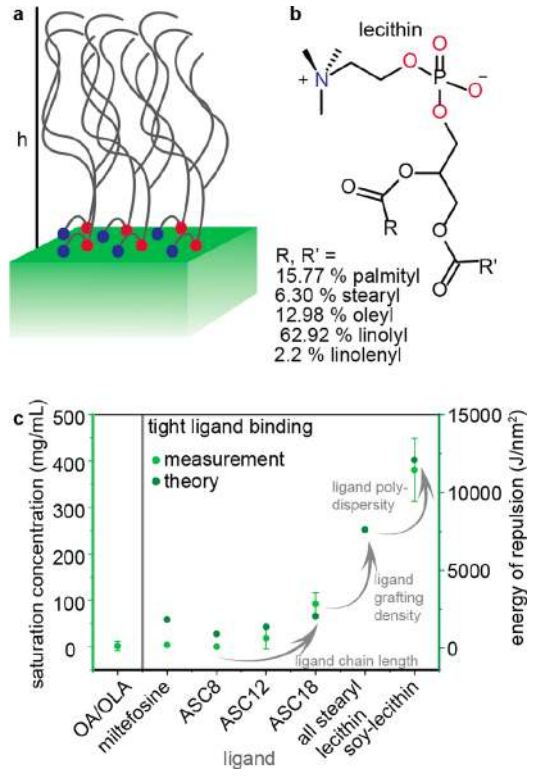

Figure 1. (a) Schematic of a lecithin-ligand brush on a $CsPbX_3$ surface; *h* indicates the brush height. (b) Chemical structure of lecithin and statistical occurrence of side chains in soy lecithin.[15] (c) Plot comparing the saturation concentration $CsPbBr_3$ NCs (ca. 7 nm) capped with different ligands: oleic acid (OA) and oleylamine (OLA), ASC8 [3-(*N*,*N*-dimethyloctylammonio)propanesulfonate] and its longer chain analogues (ASC12 and ASC18, having C12 and C18 carbon chains in place of octyl, see also an earlier study in ref 14k). The highest concentration of above 400 mg/mL (inorganic content per mL of toluene) is obtained with soy lecithin as a combined result of its higher chain length and natural lengths dispersity and, comparatively to all other studied ligands, higher grafting density (two vs one long chains per headgroup; i.e., 3.6 vs 2 tails/nm^2). For comparison, ACS18-capped NCs exhibit a saturated concentration of ca. 90 mg/mL.

RESULTS AND DISCUSSION

Soy lecithin is an inexpensive, natural, zwitterionic phospholipid which contains a physiological mixture of saturated and unsaturated long hydrocarbon chains (total of five, Figure 1b), two per molecule. Hence, it can be viewed as a polydisperse ligand. The choice of lecithin was inspired, on one hand, by our earlier studies of other zwitterionic long-chain molecules as strongly binding ligands[14k] and, on the other hand, by insights from polymer physics. To achieve highly concentrated colloids the NC−NC repulsion—typically and in this study of purely steric nature[18]—needs to be maximized. Ligand-covered NC surfaces can be viewed as brush-like structures (Figure 1a). Details of modeling the ligand−ligand repulsion between two NC surfaces can be found in the SI, Table S1 and Figures S1 and S2. The repulsion between polymer brushes has been studied extensively by De Gennes[19] and others.[20] The classical model considers these brushes as made up from stretched chains, permanently attached to an infinite, flat surface,[20,21] which are valid assumptions for lecithin-capped $CsPbBr_3$ NCs due to static ligand binding (confirmed by NMR, see discussion later in the text) and their cuboidal shape. According to classical, self-consistent mean field theory the factors which increase the energy of repulsion and thus the energy barrier for aggregation are tight binding, long chains, high grafting density,[22] and ligand chain polydispersity.[21] Calculated energy of repulsion vs number of hydrocarbons reproduces the slope obtained in the logarithmic plot of the experimental saturation concentration vs number of hydrocarbons (Figure S3). We note that we have thus far ignored the effect of the ligand interpenetration (gain in enthalpy upon aggregation due to van der Waals ligand−ligand interaction) that counteracts the steric repulsion.

Interpenetration of ligands explains the lower solubility of stearyl-ASC18 compared to oleyl-ACS18 (Figure S3). Similar effects of the ligand sterics have been observed on smaller, quasispherical NCs (CdSe, Fe_2O_3, Ag, etc.).[23] For sufficiently long chains the overall impact of interdigitation on the system's free energy will level off, as commonly observed with polymers.[24] In fact, both the experiment and the calculations agree on the grafting density and ligand-chain distribution as the factors able to boost the $CsPbBr_3$ NC−NC repulsion well beyond the impact of chain length. Soy lecithin is a natural ligand system that harnesses all three components (Figure 1c). Our results on $CsPbBr_3$ NCs and recent work by others on CdSe NCs[25] point to a rather unexplored potential of ligand systems comprising the same headgroup and a mixture of different hydrocarbon tails.

Highly concentrated colloids of lecithin-covered $CsPbBr_3$ NCs retain a fully dispersed state without noticeable aggregation for at least 1 month, as can be readily seen by the Tindall effect (Figure S4) and confirmed by dynamic light scattering (DLS, Figures S5 and S6). They can be centrifuged at 29 500*g* for 1 h without noticeable precipitation. At the other extreme, in very dilute solutions (Figure 2a and 2b, right), factors such as chain length become less important due to decreased collision probability. The tight binding of the ligand, however, gains a pivotal role as it counteracts dilution-favored desorption of the ligands (leading to NC degradation as well). The PL peak positions and PL QY values are retained upon deep dilution (Figure S7).

DOI: 10.1021/jacs.9b09969
J. Am. Chem. Soc. 2019, 141, 19839−19849

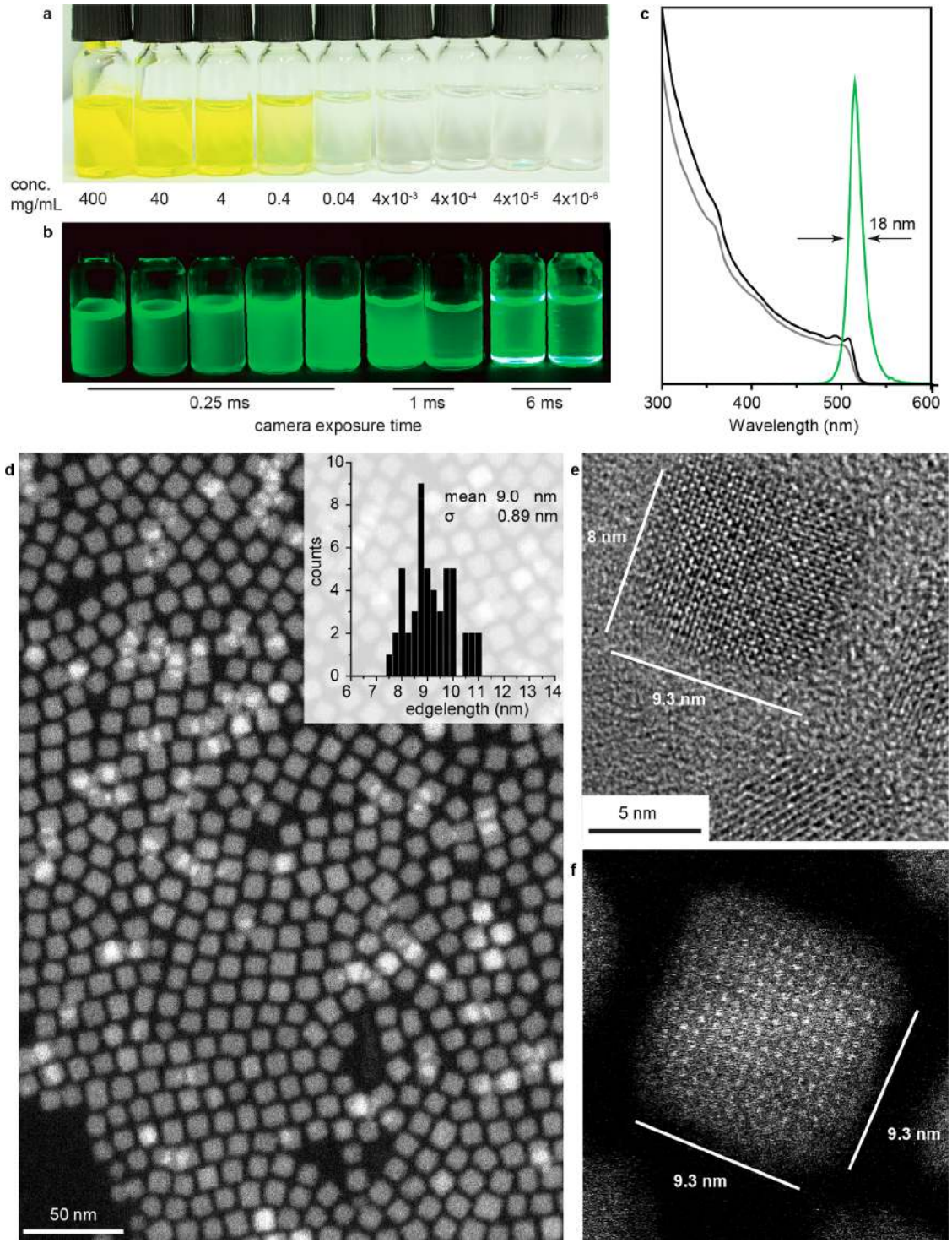

Figure 2. (a and b) Vials containing lecithin-covered ~8 nm $CsPbBr_3$ NCs at various concentrations (indicated on the figure) under day light and UV light, respectively. (c) Typical absorption spectra (gray, as synthesized; black, fraction 8) and emission spectrum (green, fraction 8), (d) high-angle annular dark field-scanning transmission electron microscopy (HAADF-STEM) image, (e) HR-TEM image, and (f) high-resolution HAADF-STEM image of $CsPbBr_3$ NCs from fraction 8 obtained by size fractioning; full size-selected series is given in Figure 3a and 3b as well as Figures S15 and S16.

Soy-lecithin-capped $CsPbX_3$ NCs were obtained at 80−150 °C in a hot-injection synthesis (see details in SI) by adapting the methodology that we previously devised for synthetic zwitterionic molecules as capping ligands. In particular, Pb−oleate, Cs−oleate, and trioctylphosphine−halogen adduct ($TOPBr_2$, $TOPCl_2$) were used as precursors, whereas octadecene was employed as a solvent (effect of halide ratio Figrue S8). The NCs crystallize into an orthorhombic perovskite lattice (*Pbnm*, Figure S9).[1d,26] NCs can be isolated by destabilizing the crude solution with acetone followed by centrifugation and redispersion in toluene. The synthesis yield can be ca. 70% (for a 130 °C, synthesis), which is about 800 mg from a 25 mL reaction scale. The loss is primarily due to incomplete precipitation at each stage. We note the practical

DOI: 10.1021/jacs.9b09969
J. Am. Chem. Soc. 2019, 141, 19839−19849

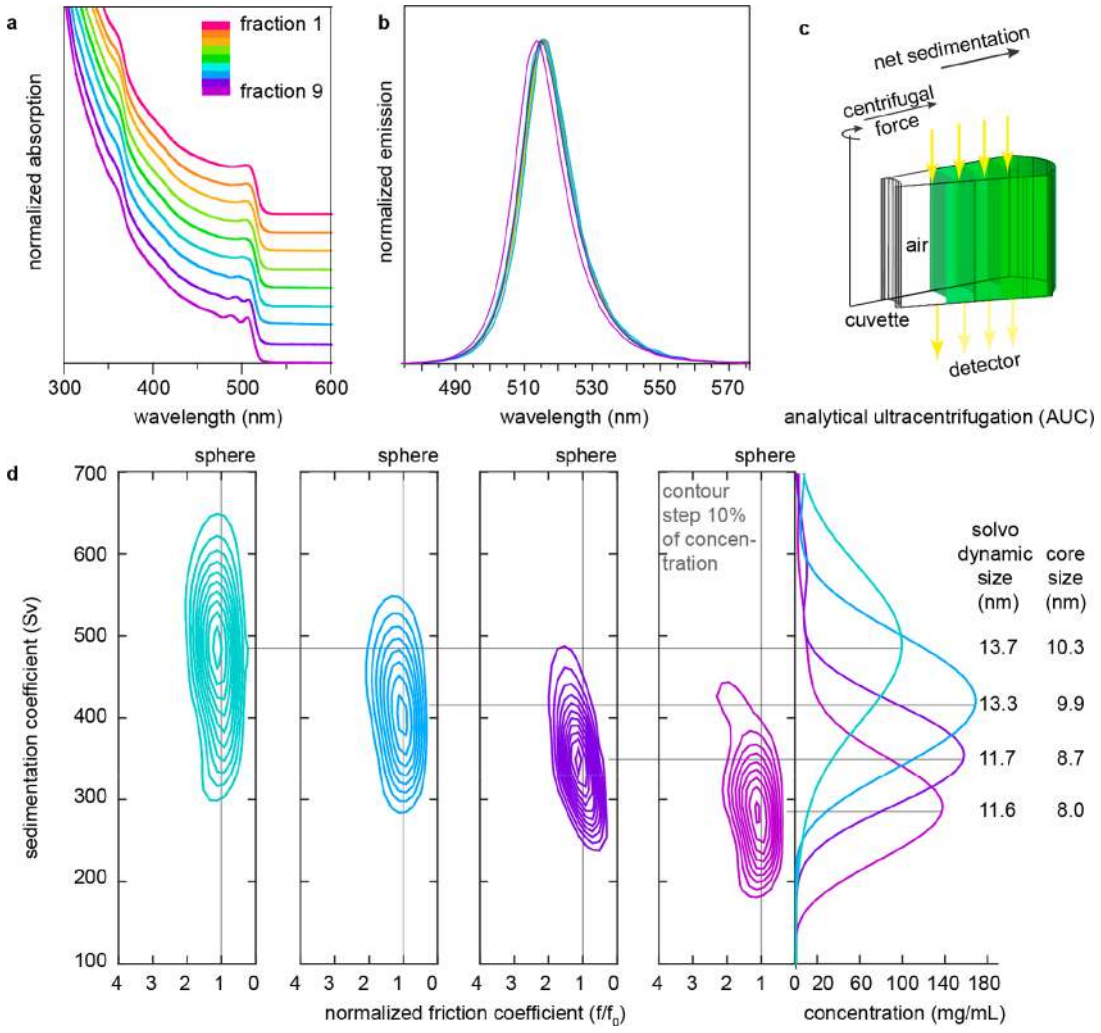

Figure 3. (a) Absorption and (b) photoluminescence spectra of size-selected fractions of $CsPbBr_3$ NCs (130 °C synthesis, 20% initial size distribution). NC size decreases with increasing fraction number. (c) Schematic of the AUC principle. (d) $C(s,f/f_0)$ distributions estimated by Sedfit from absorbance scans at 500 nm for fractions 6–9 (these fractions together sum up to 59% of the whole ensemble). Unit Sv "Svedberg" is equal to 10^{-13} s. From the distributions, solvodynamic particle size and core size were calculated and tabulated on the right. Core size refers to the average edge length of the NC. Results are tabulated in Table S4.

utility of perovskite NCs is often handicapped by the low synthesis yields caused by the losses at the isolation and purification stages, not by the initial precursor-to-NC conversion. For instance, 90% of NCs are typically lost in conventional OA/OLA synthesis due to the desorption of OA/OLA coating and NC aggregation. With zwitterionic ligands, on the contrary, up to 80% of NCs can be obtained in the form of well-purified colloids.[14k] In this regard, lecithin is a similarly efficient ligand yet with its own specifics caused by drastically enhanced colloidal stabilization. For instance, running the synthesis at the concentrations of reagents commensurate with conventional OA/OLA synthesis (i.e., five times lower than we report here) yields colloids that are hard to destabilize by acetone.

Lecithin-capped NCs fully retain their spectral characteristics after intense purification by repetitive precipitation with diverse nonsolvents under ambient conditions and after prolonged storage (Figure S10). We note that all results presented in this work are obtained for samples that were at least several weeks old. Efficient ligand binding and ligand retention upon isolation is directly confirmed by NMR spectroscopy and thermal gravimetric analysis (TGA). The ^{1}H and ^{31}P NMR spectra of lecithin-covered NCs show severe line broadening compared to lecithin reference spectra and spectra of decomposed NCs (Figures S11 and S12). Decomposition of NCs was conducted by mixing a concentrated colloid with d^6-DMSO. A plausible reason for the line broadening is the increase of the ligand's rotational correlation time due to association with the NCs. Association of the ligand molecules with each other into micelles, an alternative cause for the reduced molecular tumbling and hence line broadening, can be excluded based on analytical ultracentrifugation (AUC) measurements, as discussed later in the text. Diffusion-ordered NMR spectroscopy (DOSY) shows an increase of the ligand's diffusion coefficient by a factor of 10 when associated with the NCs (Figure S13). This is in agreement with values previously seen with other zwitterionic ligands (see ref 14k and Table S2). The NC size received from DOSY, assuming tight binding of the ligands, is commensurate with NC sizes determined by TEM or DLS (Table S2). The combination of these arguments suggests the absence of free organic solutes. With the TGA weight loss of ca. 25% (at 300 °C, Figure S14), one can estimate ligand surface densities of ca. 1.8 nm^{-2}. This value is close to that obtained with single-chain zwitterionic ligands such as ASC18 (ca. 2.0

DOI: 10.1021/jacs.9b09969
J. Am. Chem. Soc. 2019, 141, 19839–19849

nm^{-2} [14k]), suggesting that bulkier lecithin molecules do not suffer from much increased sterical encumbrance at the NC surface.

The typical absorption spectrum for $CsPbBr_3$ NCs synthesized at 130 °C is shown in Figure 2c (gray line). Such colloids are characterized by the standard size deviation of ca. 20%. For obtaining practical quantities of narrowly dispersed NCs (size distribution below 10%) we employed a so-called size-selective precipitation technique, extensively used in the past for conventional semiconductor NCs (InP, CdSe, CdTe).[27] Size fractioning is conducted by the gradual destabilization of a colloid with a nonsolvent and collection of each fraction by centrifugation. High concentrations and stable surface capping are imperative for an overall practicality of this approach. So-obtained NCs exhibit better-resolved excitonic features in the absorption spectra, as follows from Figure 2c (black curve), showing fraction 8 in this specific case, comprising 16 wt % of the initial ensemble. Electron microscopy reveals a uniform cuboid shape, mean NC size of ∼9 nm, and confirms monodispersity of these NCs (ca. 9.9% of size distribution). Monodisperse NC colloids with a mean NC size precisely adjustable in the range of 6−10 nm can be obtained by combining the effect of the synthesis temperature (higher for larger sizes) and size-selective precipitation (Figures S15 and S16, Table S3). For smaller NCs (<8 nm), which fall into strong and intermediate quantum confinement regimes,[28] the benefits of size selection on the sharpening of absorption spectra and narrowing PL lines are most pronounced. At larger sizes, PL bands are already limited by the homogeneous line width,[29] as can be seen from the spectral indistinguishability of fractions 1−8 (Figure 3b). Absorbance spectra often are less subjected to homogeneous broadening and hence render a better estimate for the spectral polydispersity of the colloids (Figure 3a).

The size distribution of the size-selected fractions (for the same 130 °C, synthesis) has been further quantified with two very distinct techniques which can probe the NCs in their native colloidal state: analytical ultracentrifugation (AUC) and small-angle X-ray scattering (SAXS). The results for fractions 6−9 are presented in Table 1 and compared to TEM data (Figure S17).

Table 1. NC Edge Lengths (in nm) Determined by Various Methods

fraction	TEM	AUC	SAXS
6	10.4 ± 0.99	10.3	
7	10.5 ± 1.2	9.9	
8	8.9 ± 0.89	8.7	7.9 × 9.1 × 9.1, σ = 6.5%, average 8.7
9	8.75 ± 0.87	8.0	7.2 × 8.2 × 8.3, σ = 6.6%, average 7.9

We employed AUC sedimentation velocity (SV) measurement for its capability in determining solvodynamic parameters of the NCs in their original dispersion.[30] In an AUC-SV experiment, the dispersion in a cell is spun at a constant speed, causing a net sedimenting movement of the NCs toward the bottom of the cell. The concentration of the nanocrystals is monitored along the cell as time progresses. Absorbance or interference optics can be utilized (Figure 3c). The evolution of the absorbance signal with space and time depends on the sedimentation of the species that absorb at a given wavelength. The evolution of the interference pattern is sensitive to all species present because their sedimentation causes a change in the refractive index of the dispersion. In our AUC-SV experiments we recorded both absorbance and interference simultaneously. A sample composed solely of NCs should have the same distribution of sedimentation coefficients derived from absorbance and interference AUC; any difference would be an indication of optically inactive species in solution (i.e., impurities). The distribution of sedimentation coefficients $C(s)$, which is determined by the particle size, shape, and density, is obtained by numerically fitting the Lamm's solution to the AUC radial profiles (Figures S18−20).[30a,31] We ran AUC on multiple fractions of the NCs. We found that for all fractions the distribution results from absorbance (550 nm) data and interference data were essentially the same (Figure S20), indicating that the particles have a high degree of purity. Representative distributions of the sedimentation coefficients are shown in Figure 3d (and others are in Figure S20). These plots clearly show that each fraction contains NCs of rather narrow size distribution and that fractionation improved size distribution.

In order to better explain the working principle of AUC we can take the example of a NCs-containing sample. The centrifugal forces that act on the NCs determine the movement of the absorbance boundary that is related to the NCs sedimentation coefficient that is proportional to their solvodynamic size. As the experiment progresses, the natural diffusion of the NCs tends to broaden the absorbance boundary whose thickness is effectively infinitely sharp at time zero and progressively can evolve to be sizable. Such evolution of the boundary is used to determine either the particle's density (assuming spherical shape) or the particle's frictional coefficient (a parameter related to the shape of the NCs, assuming a known density).[30a−c] In the analysis of the NCs described here we assume a frictional coefficient of a cube (f/f_0 = 1.05); this allowed us to calculate the density for the NCs. As explained in ref 30a, the simultaneous knowledge of the NCs solvodynamic radius (from the sedimentation coefficient) and the overall particle density allowed us to calculate the size of the inorganic core of the NCs. Overall, the core sizes found in AUC agree quantitatively with the edge lengths retrieved from HR-TEM and SAXS (see Table 1). In addition, we can also conclude that the samples are free from known impurities for these NCs (such as Cs_4PbBr_6, $CsPb_2Br_5$, $PbBr_2$, CsBr, delaminated Ruddleston−Popper phases, organic micelles, etc.) as AUC at 500 nm leads to identical results to AUC at 335 nm or AUC run in interference mode. Any of the impurities named above would have led to additional contributions to the AUC distributions.

Colloids of NCs with less than 10% polydispersity are highly suited for analysis with small angle X-ray scattering (SAXS). Size- and shape-dependent scattering features can thus be identified and interpreted, as we illustrate here for toluene solutions of lecithin-capped $CsPbBr_3$ NCs (fractions 8 and 9 from 130 °C, synthesis). Colloids were filled in a flow cell capillary, followed by the SAXS measurements at a synchrotron source (see SI section 4.5 for details). After applying intensity and background corrections, the scattering traces all showed clear features of form factor scattering and were hence compared to analytical models.[32] Additionally, the shape was reconstructed using SASHEL, a model-free Monte Carlo 3D fitting algorithm, which operates without prior assumptions.[33] The results of both methods are shown in Figures 4 and S21 for the NCs of fractions 8 and 9, respectively.

In the analytical model, an oblate cuboid with dimensions 7.99 × 9.27 × 9.27 nm (i.e., aspect ration of 0.86) and 6.43% relative polydispersity was found to most closely represent the NCs of fraction 8. Alternative models such as monodisperse

DOI: 10.1021/jacs.9b09969
J. Am. Chem. Soc. 2019, 141, 19839−19849

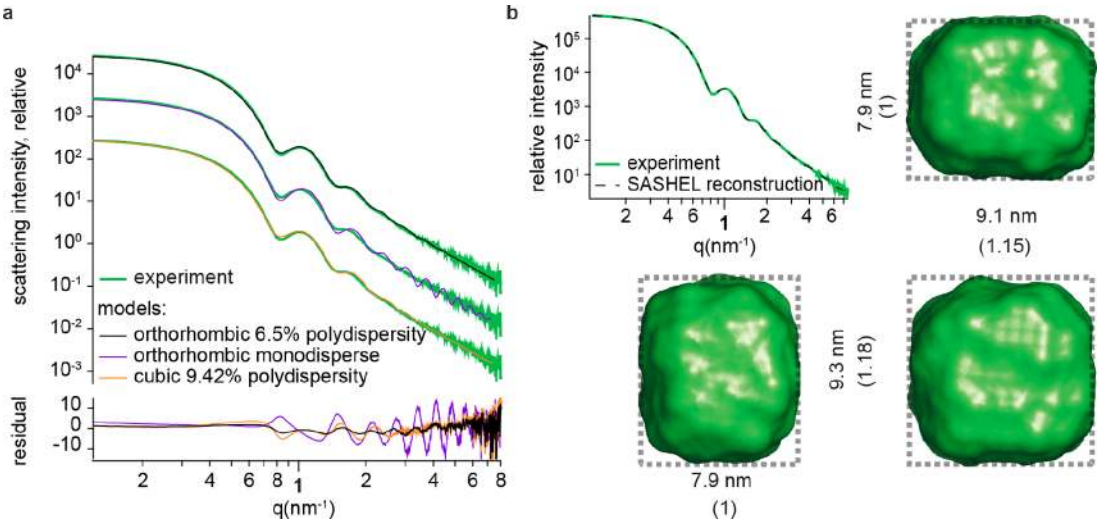

Figure 4. (a) SAXS traces of NCs from fraction 8 (green) fitted with a monodisperse orthorhombic (violet) and polydisperse cubic (orange) and orthorhombic (black) models. Best fit was found for an orthorhombic model with 6.5% polydispersity on the edge lengths (fitting results Table S5). (b) Model-free fit of the small angle scattering data along with the NC shape that allowed for the a full 3D reconstruction, shown from 3 sides. Shape found from reconstruction of the scattering pattern agrees with the best-fit model, TEM statistics (Figure 2 d–f), and AUC data (Figure 3d). Measurements and fittings for NCs from fraction 9 can be found in Figure S21.

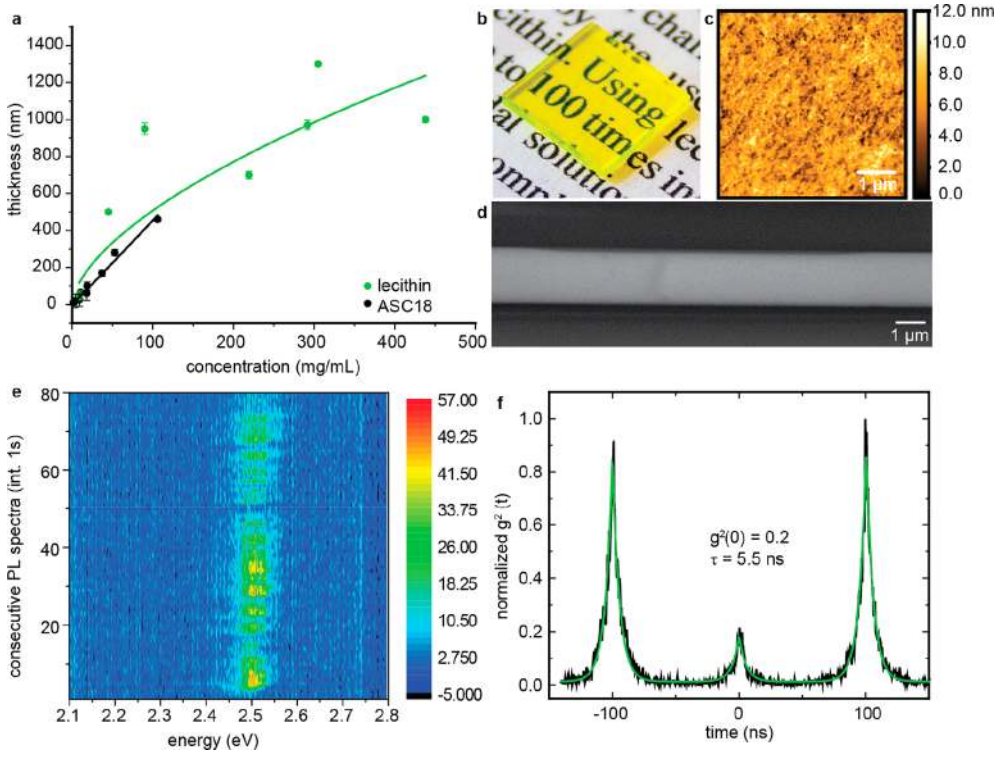

Figure 5. (a) Film thickness (AFM) under identical spin-coating conditions as a function of ink concentration (underlying AFM images Figures S22 and S23). (Green) Films made from toluene solutions of lecithin-capped $CsPbBr_3$ NCs and (black) films from toluene solutions of ASC18-capped $CsPbBr_3$ NCs. Error bars indicate film roughness. Lines are power-law fits. For the lecithin NCs the power is 0.5. (b) Photo of a 1 × 1 cm film 1 μm thick showing optical transparency; (c) AFM scan of a 1 μm thick film with roughness less than 13 nm; (d) SEM image of an identically prepared film showing long-range thickness homogeneity; (e) 80 consecutive spectra of a single lecithin-covered $CsPbBr_3$ NC showing spectral stability due to good ligand passivation; (f) normalized correlogram indicating a single emitter is measured.

cuboids and cubes with 9.4% relative polydispersity did not reproduce the measured scattering traces as closely, as can be seen from the residuals in Figure 4a. Full reconstruction yielded a cuboidal NC shape of 7.9 × 9.1 × 9.3 nm for NCs of fraction 8 (Figures 4b).

Retention of colloidal, structural, and optical integrity over a broad concentration range of $CsPbX_3$ NCs, i.e., from 400 mg/mL down to few ng/mL, will have diverse practical implications. In the following, we showcase two instances of immense practical utility of ultraconcentrated as well as ultradilute colloids of $CsPbX_3$ NCs.

DOI: 10.1021/jacs.9b09969
J. Am. Chem. Soc. 2019, 141, 19839–19849

Highly concentrated colloids can be used as inks for one-step deposition of thick, smooth, optically clear films by spin coating. The thickness of the film can be readily adjusted by the concentration of the colloid to above 1 μm while maintaining a roughness of just 15 nm (Figure 5a–d, Figures S22 and S23). Previously, micrometer-thick perovskite NC films were obtained mostly by stepwise deposition with intermittent consolidation steps[8d,14c] or by filling of a scaffold structure.[6a,34] The experimental thickness vs concentration dependence—while linear in ASC18-covered NCs (black)—can be approximated with a square root law for lecithin-covered NCs (green), although an increase with the power of 1/3 would be generally expected. This deviation can be rationalized by the variation of solution properties such as viscosity, vapor pressure, or contact angle at high volumetric loadings,[35] which are critical to the spin-coating process. In particular, higher viscosity leads to thicker than expected films. Importantly, these films exhibit excellent optical clarity, indicative of their aggregation-free deposition and high PL QYs of ca. 30% at all thicknesses. Such thick films may find applications in the next-generation displays with NC films serving as both light filters and emitters[3a,i,17] or as scintillators for detecting X-rays and gamma-rays.[6,9]

Ultradilute colloids are also in great demand. For example, dilution to the ng/mL level is necessary for obtaining sparsely distributed NCs upon deposition and solvent evaporation. In particular, dilutions which result in the average NC-to-NC separation by several micrometers are ideally suited for single NC spectroscopy with typical microphotoluminescence setups. As discussed above, labile ligand shells rapidly lead to the loss of colloidal state and NC aggregation upon such severe dilution due to ligand desorption. We therefore tested the durability of lecithin-capped $CsPbBr_3$ NCs for obtaining single-photon emission at room temperature (Figure 5e and 5f), moreover, by conducting all steps under ambient conditions. Despite the presence of PL blinking as usually reported for these NCs, the PL is stable for several tens of seconds and without significant PL blue shift (typical for perovskite NCs).[7j,29a,36] Second-order correlation measurements attest single-photon emission with the characteristic antibunching behavior and a good single-photon purity ($g2(0) \approx 0.2$), further confirming a non-aggregated, intact state of these NCs.

CONCLUSIONS

We found that soy lecithin—an inexpensive, natural, mass-produced zwitterionic phospholipid—makes for an effective capping ligand for the synthesis of colloidal $CsPbX_3$ NCs. Most importantly, it imparts high colloidal stability in a broad range of NC concentrations (from few ng/mL to above 400 mg/mL). Tight ligand binding, high grafting density, long chains, and ligand polydispersity are the key contributors of the effectiveness of this ligand. High synthesis yield and robustness of the colloids allow for facile size fractioning of the colloids, yielding practical quantities of monodisperse NCs with mean particle size tunable in the range of 6–10 nm. The size, shape, and size distribution of so-obtained NCs have been thoroughly examined with TEM, SAXS, and AUC techniques. In particular, the shape of these NCs have been confirmed to be oblate cuboids with a small aspect ratio of ca. 0.86.

An immense practical utility of such ultraconcentrated and ultradilute colloids has been illustrated by two showcase experiments. First, we have shown a one-step deposition of thick (up to 1.5 μm) NC films by spin coating. Such films exhibit excellent optical clarity while retaining bright fluorescence. Second, such colloids are also versatile inks for obtaining highly dilute NC systems as required for single-dot spectroscopy. Single-photon emission with pronounced photon antibunching has thus been readily observed.

ASSOCIATED CONTENT

Supporting Information

The Supporting Information is available free of charge at https://pubs.acs.org/doi/10.1021/jacs.9b09969.

Experimental methods and supplementary figures (PDF)

AUTHOR INFORMATION

Corresponding Author

*mvkovalenko@ethz.ch

ORCID

Frank Krumeich: 0000-0001-5625-1536

Maryna I. Bodnarchuk: 0000-0001-6597-3266

Francesco Stellacci: 0000-0003-4635-6080

Maksym V. Kovalenko: 0000-0002-6396-8938

Notes

The authors declare no competing financial interest.

ACKNOWLEDGMENTS

This work was financially supported by the Swiss Federal Commission for Technology and Innovation (CTI-No. 18614.1 PFNM-NM) and, in part, by the European Union through the FP7 (ERC Starting Grant NANOSOLID, grant agreement No. [306733]) and through the Horizon 2020 Research and Innovation Programme (grant agreement No. [819740], project SCALE-HALO). Q.O. and F.S. gratefully acknowledge support from the Swiss National Science Foundation (SNSF) (Grant No. 200020_185062). This project received funding from the EU-H2020 Research and Innovation Programme under grant agreement no. 654360 having benefitted from access to the Austrian SAXS beamline provided by TUG@Elettra in Trieste, Italy, within the framework of the NFFA-Europe Transnational Access Activity. The authors thank the Scientific Center for Optical and Electron Microscopy (ScopeM) at ETH Zurich and the Empa Electron Microscopy Center for use of their facilities.

REFERENCES

(1) (a) Schmidt, L. C.; Pertegas, A.; Gonzalez-Carrero, S.; Malinkiewicz, O.; Agouram, S.; Minguez Espallargas, G.; Bolink, H. J.; Galian, R. E.; Perez-Prieto, J. Nontemplate Synthesis of $CH_3NH_3PbBr_3$ Perovskite Nanoparticles. *J. Am. Chem. Soc.* **2014**, *136*, 850–853. (b) Protesescu, L.; Yakunin, S.; Bodnarchuk, M. I.; Krieg, F.; Caputo, R.; Hendon, C. H.; Yang, R. X.; Walsh, A.; Kovalenko, M. V. Nanocrystals of Cesium Lead Halide Perovskites ($CsPbX_3$, X = Cl, Br, and I): Novel Optoelectronic Materials Showing Bright Emission with Wide Color Gamut. *Nano Lett.* **2015**, *15*, 3692–6. (c) Protesescu, L.; Yakunin, S.; Bodnarchuk, M. I.; Bertolotti, F.; Masciocchi, N.; Guagliardi, A.; Kovalenko, M. V. Monodisperse Formamidinium Lead Bromide Nanocrystals with Bright and Stable Green Photoluminescence. *J. Am. Chem. Soc.* **2016**, *138*, 14202–14205. (d) Swarnkar, A.; Chulliyil, R.; Ravi, V. K.; Irfanullah, M.; Chowdhury, A.; Nag, A. Colloidal CsPbBr3 Perovskite Nanocrystals: Luminescence beyond Traditional Quantum Dots. *Angew. Chem., Int. Ed.* **2015**, *54*, 15424–15428. (e) Huang, H.; Polavarapu, L.; Sichert, J. A.; Susha, A. S.; Urban, A. S.; Rogach, A. L. Colloidal Lead Halide Perovskite Nanocrystals: Synthesis, Optical Properties and Applications. *NPG Asia Mater.* **2016**, *8*, e328–e328. (f) Kovalenko, M. V.; Protesescu, L.; Bodnarchuk, M. I. Properties and Potential Optoelectronic Applications of Lead Halide Perovskite Nanocrystals. *Science* **2017**, *358*, 745–

DOI: 10.1021/jacs.9b09969
J. Am. Chem. Soc. 2019, 141, 19839–19849

750. (g) Zhang, J.; Yang, X. K.; Deng, H.; Qiao, K. K.; Farooq, U.; Ishaq, M.; Yi, F.; Liu, H.; Tang, J.; Song, H. S. Low-Dimensional Halide Perovskites and Their Advanced Optoelectronic Applications. *Nano-Micro Lett.* **2017**, *9*, 36−62. (h) Li, X.; Cao, F.; Yu, D.; Chen, J.; Sun, Z.; Shen, Y.; Zhu, Y.; Wang, L.; Wei, Y.; Wu, Y.; Zeng, H. All Inorganic Halide Perovskites Nanosystem: Synthesis, Structural Features, Optical Properties and Optoelectronic Applications. *Small* **2017**, *13*, 1603996−1604020. (i) Akkerman, Q. A.; Raino, G.; Kovalenko, M. V.; Manna, L. Genesis, Challenges and Opportunities for Colloidal Lead Halide Perovskite Nanocrystals. *Nat. Mater.* **2018**, *17*, 394−405. (j) Adinolfi, V.; Peng, W.; Walters, G.; Bakr, O. M.; Sargent, E. H. The Electrical and Optical Properties of Organometal Halide Perovskites Relevant to Optoelectronic Performance. *Adv. Mater.* **2018**, *30*, 1700764−1700777. (k) Zhao, Y.; Li, J.; Dong, Y.; Song, J. Synthesis of Colloidal Halide Perovskite Quantum Dots/Nanocrystals: Progresses and Advances. *Isr. J. Chem.* **2019**, *59*, 649−660. (l) Shamsi, J.; Urban, A. S.; Imran, M.; De Trizio, L.; Manna, L. Metal Halide Perovskite Nanocrystals: Synthesis, Post-Synthesis Modifications, and Their Optical Properties. *Chem. Rev.* **2019**, *119*, 3296−3348. (m) Zheng, X. P.; Hou, Y.; Sun, H. T.; Mohammed, O. F.; Sargent, E. H.; Bakr, O. M. Reducing Defects in Halide Perovskite Nanocrystals for Light-Emitting Applications. *J. Phys. Chem. Lett.* **2019**, *10*, 2629−2640. (n) Dutta, A.; Pradhan, N. Phase-Stable Red-Emitting $CsPbI_3$ Nanocrystals: Successes and Challenges. *ACS Energy Lett.* **2019**, *4*, 709−719.

(2) (a) Giansante, C.; Infante, I. Surface Traps in Colloidal Quantum Dots: A Combined Experimental and Theoretical Perspective. *J. Phys. Chem. Lett.* **2017**, *8*, 5209−5215. (b) Huang, H.; Bodnarchuk, M. I.; Kershaw, S. V.; Kovalenko, M. V.; Rogach, A. L. Lead Halide Perovskite Nanocrystals in the Research Spotlight: Stability and Defect Tolerance. *ACS Energy Lett.* **2017**, *2*, 2071−2083. (c) Motti, S. G.; Meggiolaro, D.; Martani, S.; Sorrentino, R.; Barker, A. J.; De Angelis, F.; Petrozza, A. Defect Activity in Metal-Halide Perovskites. *Adv. Mater.* **2019**, *31*, 1901183.

(3) (a) Kovalenko, M. V.; Bodnarchuk, M. I. Lead Halide Perovskite Nanocrystals: From Discovery to Self-assembly and Applications. *Chimia* **2017**, *71*, 461−470. (b) Zhao, X.; Ng, J. D. A.; Friend, R. H.; Tan, Z.-K. Opportunities and Challenges in Perovskite Light-Emitting Devices. *ACS Photonics* **2018**, *5*, 3866−3875. (c) Van Le, Q.; Jang, H. W.; Kim, S. Y. Recent Advances toward High-Efficiency Halide Perovskite Light emitting diodes Review and Perspective. *Small Methods* **2018**, *2*, 1700419−1700437. (d) Chiba, T.; Kido, J. Lead Halide Perovskite Quantum Dots for Light Emitting Devices. *J. Mater. Chem. C* **2018**, *6*, 11868. (e) Zhang, F.; Song, J.; Han, B.; Fang, T.; Li, J.; Zeng, H. High-Efficiency Pure-Color Inorganic Halide Perovskite Emitters for Ultrahigh-Definition Displays: Progress for Backlighting Displays and Electrically Driven Devices. *Small Methods* **2018**, *2*, 1700382−1700391. (f) Kim, Y.-H.; Kim, S.; Jo, S. H.; Lee, T.-W. Metal Halide Perovskites: From Crystal Formations to Light-Emitting-Diode Applications. *Small Methods* **2018**, *2*, 1800093−1800114. (g) Chang, S.; Bai, Z.; Zhong, H. In Situ Fabricated Perovskite Nanocrystals: A Revolution in Optical Materials. *Adv. Opt. Mater.* **2018**, *6*, 1800380−1800399. (h) Chen, N.; Bai, Z.; Wang, Z.; Ji, H.; Liu, R.; Cao, C.; Wang, H.; Jiang, F.; Zhong, H. Low Cost Quantum Dot Film based Wide Color Gamut Backlight Unit for LCD TVs. *Dig. Tech. Pap. - Soc. Inf. Disp. Int. Symp.* **2018**, *49*, 1657−1659. (i) Yoon, H. C.; Lee, H.; Kang, H.; Oh, J. H.; Do, Y. R. Highly Efficient Wide-Color-Gamut QD-Emissive LCDs using Red and Green Perovskite Core/Shell QDs. *J. Mater. Chem. C* **2018**, *6*, 13023−13033. (j) Lu, M.; Zhang, Y.; Wang, S.; Guo, J.; Yu, W. W.; Rogach, A. L. Metal Halide Perovskite Light-Emitting Devices: Promising Technology for Next-Generation Displays. *Adv. Funct. Mater.* **2019**, *29*, 1902008−1902043. (k) He, Z.; Zhang, C.; Dong, Y.; Wu, S.-T. Emerging Perovskite Nanocrystals-Enhanced Solid-State Lighting and Liquid-Crystal Displays. *Crystals* **2019**, *9*, 59.

(4) (a) Yakunin, S.; Protesescu, L.; Krieg, F.; Bodnarchuk, M. I.; Nedelcu, G.; Humer, M.; De Luca, G.; Fiebig, M.; Heiss, W.; Kovalenko, M. V. Low-threshold Amplified Spontaneous Emission and Lasing from Colloidal Nanocrystals of Caesium Lead Halide Perovskites. *Nat. Commun.* **2015**, *6*, 8056−8064. (b) Stylianakis, M. M.; Maksudov, T.; Panagiotopoulos, A.; Kakavelakis, G.; Petridis, K. Inorganic and Hybrid Perovskite Based Laser Devices: A Review. *Materials* **2019**, *12*, 859. (c) Zhang, Y.; Lim, C.-K.; Dai, Z.; Yu, G.; Haus, J. W.; Zhang, H.; Prasad, P. N. Photonics and Optoelectronics using Nano-Structured Hybrid Perovskite Media and their Optical Cavities. *Phys. Rep.* **2019**, *795*, 1−51.

(5) (a) Wu, Y.; Li, X.; Wei, Y.; Gu, Y.; Zeng, H. Perovskite Photodetectors with both Visible-Infrared Dual-Mode Response and Super-Narrowband Characteristics towards Photo-Communication Encryption Application. *Nanoscale* **2018**, *10*, 359−365. (b) Mei, S.; Liu, X.; Zhang, W.; Liu, R.; Zheng, L.; Guo, R.; Tian, P. High-Bandwidth White-Light System Combining a Micro-LED with Perovskite Quantum Dots for Visible Light Communication. *ACS Appl. Mater. Interfaces* **2018**, *10*, 5641−5648. (c) Zhang, Y.; Wang, L.; Wang, K.; Wong, K. S.; Wu, K. Recent Advances in the Hardware of Visible Light Communication. *IEEE Access* **2019**, *7*, 91093−91104. (d) Cen, G.; Liu, Y.; Zhao, C.; Wang, G.; Fu, Y.; Yan, G.; Yuan, Y.; Su, C.; Zhao, Z.; Mai, W. Atomic-Layer Deposition-Assisted Double-Side Interfacial Engineering for High-Performance Flexible and Stable $CsPbBr_3$ Perovskite Photodetectors toward Visible Light Communication Applications. *Small* **2019**, *15*, 1902135.

(6) (a) Chen, Q.; Wu, J.; Ou, X.; Huang, B.; Almutlaq, J.; Zhumekenov, A. A.; Guan, X.; Han, S.; Liang, L.; Yi, Z.; Li, J.; Xie, X.; Wang, Y.; Li, Y.; Fan, D.; Teh, D. B. L.; All, A. H.; Mohammed, O. F.; Bakr, O. M.; Wu, T.; Bettinelli, M.; Yang, H.; Huang, W.; Liu, X. All-Inorganic Perovskite Nanocrystal Scintillators. *Nature* **2018**, *561*, 88−93. (b) Maddalena, F.; Tjahjana, L.; Xie, A.; Arramel; Zeng, S.; Wang, H.; Coquet, P.; Drozdowski, W.; Dujardin, C.; Dang, C.; Birowosuto, M. Inorganic, Organic, and Perovskite Halides with Nanotechnology for High−Light Yield X- and γ-ray Scintillators. *Crystals* **2019**, *9*, 88−117.

(7) (a) Raino, G.; Nedelcu, G.; Protesescu, L.; Bodnarchuk, M. I.; Kovalenko, M. V.; Mahrt, R. F.; Stoferle, T. Single Cesium Lead Halide Perovskite Nanocrystals at Low Temperature: Fast Single-Photon Emission, Reduced Blinking, and Exciton Fine Structure. *ACS Nano* **2016**, *10*, 2485−2490. (b) Fu, M.; Tamarat, P.; Huang, H.; Even, J.; Rogach, A. L.; Lounis, B. Neutral and Charged Exciton Fine Structure in Single Lead Halide Perovskite Nanocrystals Revealed by Magneto-optical Spectroscopy. *Nano Lett.* **2017**, *17*, 2895−2901. (c) Fu, M.; Tamarat, P.; Trebbia, J. B.; Bodnarchuk, M. I.; Kovalenko, M. V.; Even, J.; Lounis, B. Unraveling Exciton-Phonon Coupling in Individual $FAPbI_3$ Nanocrystals Emitting near-infrared Single Photons. *Nat. Commun.* **2018**, *9*, 3318−3328. (d) Tong, Y.; Fu, M.; Bladt, E.; Huang, H.; Richter, A. F.; Wang, K.; Muller-Buschbaum, P.; Bals, S.; Tamarat, P.; Lounis, B.; Feldmann, J.; Polavarapu, L. Chemical Cutting of Perovskite Nanowires into Single-Photon Emissive Low-Aspect-Ratio $CsPbX_3$ (X = Cl, Br, I) Nanorods. *Angew. Chem., Int. Ed.* **2018**, *57*, 16094−16098. (e) Li, B.; Huang, H.; Zhang, G. F.; Yang, C. G.; Guo, W. L.; Chen, R. Y.; Qin, C. B.; Gao, Y.; Biju, V. P.; Rogach, A. L.; Xiao, L. T.; Jia, S. T. Excitons and Biexciton Dynamics in Single $CsPbBr_3$ Perovskite Quantum Dots. *J. Phys. Chem. Lett.* **2018**, *9*, 6934−6940. (f) Becker, M. A.; Scarpelli, L.; Nedelcu, G.; Raino, G.; Masia, F.; Borri, P.; Stoferle, T.; Kovalenko, M. V.; Langbein, W.; Mahrt, R. F. Long Exciton Dephasing Time and Coherent Phonon Coupling in $CsPbBr_2Cl$ Perovskite Nanocrystals. *Nano Lett.* **2018**, *18*, 7546−7551. (g) Becker, M. A.; Vaxenburg, R.; Nedelcu, G.; Sercel, P. C.; Shabaev, A.; Mehl, M. J.; Michopoulos, J. G.; Lambrakos, S. G.; Bernstein, N.; Lyons, J. L.; Stoferle, T.; Mahrt, R. F.; Kovalenko, M. V.; Norris, D. J.; Raino, G.; Efros, A. L. Bright Triplet Excitons in Caesium Lead Halide Perovskites. *Nature* **2018**, *553*, 189−193. (h) Utzat, H.; Sun, W.; Kaplan, A. E. K.; Krieg, F.; Ginterseder, M.; Spokoyny, B.; Klein, N. D.; Shulenberger, K. E.; Perkinson, C. F.; Kovalenko, M. V.; Bawendi, M. G. Coherent Single-Photon Emission from Colloidal Lead Halide Perovskite Quantum Dots. *Science* **2019**, *363*, 1068−1072. (i) Tamarat, P.; Bodnarchuk, M. I.; Trebbia, J. B.; Erni, R.; Kovalenko, M. V.; Even, J.; Lounis, B. The Ground Exciton State of Formamidinium Lead Bromide Perovskite Nanocrystals is a Singlet Dark State. *Nat. Mater.* **2019**, *18*, 717−724. (j) Raino, G.; Landuyt, A.;

DOI: 10.1021/jacs.9b09969
J. Am. Chem. Soc. 2019, 141, 19839−19849

Krieg, F.; Bernasconi, C.; Ochsenbein, S. T.; Dirin, D. N.; Bodnarchuk, M. I.; Kovalenko, M. V. Underestimated Effect of a Polymer Matrix on the Light Emission of Single $CsPbBr_3$ Nanocrystals. *Nano Lett.* **2019**, *19*, 3648−3653.

(8) (a) NREL Best Research-Cell Efficiency Chart; https://www.nrel.gov/pv/cell-efficiency.html (accessed Aug 26, 2019). (b) Swarnkar, A.; Marshall, A. R.; Sanehira, E. M.; Chernomordik, B. D.; Moore, D. T.; Christians, J. A.; Chakrabarti, T.; Luther, J. M. Quantum Dot−Induced Phase Stabilization of a-$CsPbI_3$ Perovskite for High-Efficiency Photovoltaics. *Science* **2016**, *354*, 92−95. (c) Sanehira, E. M.; Marshall, A. R.; Christians, J. A.; Harvey, S. P.; Ciesielski, P. N.; Wheeler, L. M.; Schulz, P.; Lin, L. Y.; Beard, M. C.; Luther, J. M. Enhanced mobility $CsPbI_3$ Quantum Dot Arrays for Record-Efficiency, High-Voltage Photovoltaic Cells. *Sci. Adv.* **2017**, *3*, eaao4204. (d) Wheeler, L. M.; Sanehira, E. M.; Marshall, A. R.; Schulz, P.; Suri, M.; Anderson, N. C.; Christians, J. A.; Nordlund, D.; Sokaras, D.; Kroll, T.; Harvey, S. P.; Berry, J. J.; Lin, L. Y.; Luther, J. M. Targeted Ligand-Exchange Chemistry on Cesium Lead Halide Perovskite Quantum Dots for High-Efficiency Photovoltaics. *J. Am. Chem. Soc.* **2018**, *140*, 10504−10513. (e) Song, Z.; Chen, C.; Li, C.; Awni, R. A.; Zhao, D.; Yan, Y. Wide-Bandgap, Low-Bandgap, and Tandem Perovskite Solar Cells. Semicond. *Semicond. Sci. Technol.* **2019**, *34*, 093001−093032. (f) Fu, H. Colloidal Metal Halide Perovskite Nanocrystals: a Promising Juggernaut in Photovoltaic Applications. *J. Mater. Chem. A* **2019**, *7*, 14357−14379.

(9) Miao, J.; Zhang, F. Recent Progress on Highly Sensitive Perovskite Photodetectors. *J. Mater. Chem. C* **2019**, *7*, 1741−1791.

(10) (a) Talapin, D. V.; Lee, J.-S.; Kovalenko, M. V.; Shevchenko, E. V. Prospects of Colloidal Nanocrystals for Electronic and Optoelectronic Applications. *Chem. Rev.* **2010**, *110*, 389−458. (b) Boles, M. A.; Ling, D.; Hyeon, T.; Talapin, D. V. The Surface Science of Nanocrystals. *Nat. Mater.* **2016**, *15*, 141−153. (c) Houtepen, A. J.; Hens, Z.; Owen, J. S.; Infante, I. On the Origin of Surface Traps in Colloidal II-VI Semiconductor Nanocrystals. *Chem. Mater.* **2017**, *29*, 752−761.

(11) (a) Weiss, E. A. Organic Molecules as Tools To Control the Growth, Surface Structure, and Redox Activity of Colloidal Quantum Dots. *Acc. Chem. Res.* **2013**, *46*, 2607−2615. (b) Ling, D. S.; Hackett, M. J.; Hyeon, T. Surface Ligands in Synthesis, Modification, Assembly and Biomedical Applications of Nanoparticles. *Nano Today* **2014**, *9*, 457−477. (c) Kagan, C. R.; Lifshitz, E.; Sargent, E. H.; Talapin, D. V. Building Devices from Colloidal Quantum Dots. *Science* **2016**, *353*, aac5523. (d) ten Brinck, S.; Infante, I. Surface Termination, Morphology, and Bright Photoluminescence of Cesium Lead Halide Perovskite Nanocrystals. *ACS Energy Lett.* **2016**, *1*, 1266−1272.

(12) (a) Ravi, V. K.; Santra, P. K.; Joshi, N.; Chugh, J.; Singh, S. K.; Rensmo, H.; Ghosh, P.; Nag, A. Origin of the Substitution Mechanism for the Binding of Organic Ligands on the Surface of $CsPbBr_3$ Perovskite Nanocubes. *J. Phys. Chem. Lett.* **2017**, *8*, 4988−4994. (b) Nenon, D. P.; Pressler, K.; Kang, J.; Koscher, B. A.; Olshansky, J. H.; Osowiecki, W. T.; Koc, M. A.; Wang, L. W.; Alivisatos, A. P. Design Principles for Trap-Free $CsPbX_3$ Nanocrystals: Enumerating and Eliminating Surface Halide Vacancies with Softer Lewis Bases. *J. Am. Chem. Soc.* **2018**, *140*, 17760−17772. (c) Bodnarchuk, M. I.; Boehme, S. C.; ten Brinck, S.; Bernasconi, C.; Shynkarenko, Y.; Krieg, F.; Widmer, R.; Aeschlimann, B.; Günther, G.; Kovalenko, M. V.; Infante, I. Rationalizing and Controlling the Surface Structure and Electronic Passivation of Cesium Lead Halide Nanocrystals. *ACS Energy Lett.* **2019**, *4*, 63−74. (d) Quarta, D.; Imran, M.; Capodilupo, A.-L.; Petralanda, U.; van Beek, B.; De Angelis, F.; Manna, L.; Infante, I.; De Trizio, L.; Giansante, C. Stable Ligand Coordination at the Surface of Colloidal $CsPbBr_3$ Nanocrystals. *J. Phys. Chem. Lett.* **2019**, *10*, 3715−3726.

(13) (a) De Roo, J.; Ibanez, M.; Geiregat, P.; Nedelcu, G.; Walravens, W.; Maes, J.; Martins, J. C.; Van Driessche, I.; Kovalenko, M. V.; Hens, Z. Highly Dynamic Ligand Binding and Light Absorption Coefficient of Cesium Lead Bromide Perovskite Nanocrystals. *ACS Nano* **2016**, *10*, 2071−81. (b) Smock, S. R.; Williams, T. J.; Brutchey, R. L. Quantifying the Thermodynamics of Ligand Binding to $CsPbBr_3$ Quantum Dots. *Angew. Chem., Int. Ed.* **2018**, *57*, 11711−11715. (c) Grisorio, R.; Di Clemente, M. E.; Fanizza, E.; Allegretta, I.; Altamura, D.; Striccoli, M.; Terzano, R.; Giannini, C.; Irimia-Vladu, M.; Suranna, G. P. Exploring the surface chemistry of cesium lead halide perovskite nanocrystals. *Nanoscale* **2019**, *11*, 986−999.

(14) (a) Koh, W.; Park, S.; Ham, Y. Phosphonic Acid Stabilized Colloidal $CsPbX_3$ (X = Br, I) Perovskite Nanocrystals and Their Surface Chemistry. *Chemistry Select* **2016**, *1*, 3479−3482. (b) Wang, C.; Chesman, A. S.; Jasieniak, J. J. Stabilizing the Cubic Perovskite Phase of $CsPbI_3$ Nanocrystals by Using an Alkyl Phosphinic Acid. *Chem. Commun.* **2017**, *53*, 232−235. (c) Swarnkar, A.; Marshall, A. R.; Sanehira, E. M.; Chernomordik, B. D.; Moore, D. T.; Christians, J. A.; Chakrabarti, T.; Luther, J. M. Quantum dot−induced phase stabilization of a-$CsPbI_3$ perovskite for high-efficiency photovoltaics. *Science* **2016**, *354*, 92−95. (d) Lu, C.; Li, H.; Kolodziejski, K.; Dun, C.; Huang, W.; Carroll, D.; Geyer, S. M. Enhanced Stabilization of inorganic Cesium Lead Triiodide ($CsPbI_3$) Perovskite Quantum Dots with Tri-Octylphosphine. *Nano Res.* **2018**, *11*, 762−768. (e) Wu, L.; Zhong, Q.; Yang, D.; Chen, M.; Hu, H.; Pan, Q.; Liu, H.; Cao, M.; Xu, Y.; Sun, B.; Zhang, Q. Improving the Stability and Size Tunability of Cesium Lead Halide Perovskite Nanocrystals Using Trioctylphosphine Oxide as the Capping Ligand. *Langmuir* **2017**, *33*, 12689−12696. (f) Liu, F.; Zhang, Y.; Ding, C.; Kobayashi, S.; Izuishi, T.; Nakazawa, N.; Toyoda, T.; Ohta, T.; Hayase, S.; Minemoto, T.; Yoshino, K.; Dai, S.; Shen, Q. Highly Luminescent Phase-Stable $CsPbI_3$ Perovskite Quantum Dots Achieving Near 100% Absolute Photoluminescence Quantum Yield. *ACS Nano* **2017**, *11*, 10373−10383. (g) Di Stasio, F.; Christodoulou, S.; Huo, N.; Konstantatos, G. Near-Unity Photoluminescence Quantum Yield in $CsPbBr_3$ Nanocrystal Solid-State Films via Postsynthesis Treatment with Lead Bromide. *Chem. Mater.* **2017**, *29*, 7663−7667. (h) Koscher, B. A.; Swabeck, J. K.; Bronstein, N. D.; Alivisatos, A. P. Essentially Trap-Free $CsPbBr_3$ Colloidal Nanocrystals by Postsynthetic Thiocyanate Surface Treatment. *J. Am. Chem. Soc.* **2017**, *139*, 6566−6569. (i) Woo, J. Y.; Kim, Y.; Bae, J.; Kim, T. G.; Kim, J. W.; Lee, D. C.; Jeong, S. Highly Stable Cesium Lead Halide Perovskite Nanocrystals through in Situ Lead Halide Inorganic Passivation. *Chem. Mater.* **2017**, *29*, 7088−7092. (j) Almeida, G.; Ashton, O. J.; Goldoni, L.; Maggioni, D.; Petralanda, U.; Mishra, N.; Akkerman, Q. A.; Infante, I.; Snaith, H. J.; Manna, L. The Phosphine Oxide Route toward Lead Halide Perovskite Nanocrystals. *J. Am. Chem. Soc.* **2018**, *140*, 14878−14886. (k) Krieg, F.; Ochsenbein, S. T.; Yakunin, S.; ten Brinck, S.; Aellen, P.; Süess, A.; Clerc, B.; Guggisberg, D.; Nazarenko, O.; Shynkarenko, Y.; Kumar, S.; Shih, C.-J.; Infante, I.; Kovalenko, M. V. Colloidal $CsPbX_3$ (X = Cl, Br, I) Nanocrystals 2.0: Zwitterionic Capping Ligands for Improved Durability and Stability. *ACS Energy Lett.* **2018**, *3*, 641−646. (l) Tan, Y.; Zou, Y.; Wu, L.; Huang, Q.; Yang, D.; Chen, M.; Ban, M.; Wu, C.; Wu, T.; Bai, S.; Song, T.; Zhang, Q.; Sun, B. Highly Luminescent and Stable Perovskite Nanocrystals with Octylphosphonic Acid as a Ligand for Efficient Light-Emitting Diodes. *ACS Appl. Mater. Interfaces* **2018**, *10*, 3784−3792. (m) Dong, Y.; Qiao, T.; Kim, D.; Parobek, D.; Rossi, D.; Son, D. H. Precise Control of Quantum Confinement in Cesium Lead Halide Perovskite Quantum Dots via Thermodynamic Equilibrium. *Nano Lett.* **2018**, *18*, 3716−3722. (n) Imran, M.; Caligiuri, V.; Wang, M.; Goldoni, L.; Prato, M.; Krahne, R.; De Trizio, L.; Manna, L. Benzoyl Halides as Alternative Precursors for the Colloidal Synthesis of Lead-Based Halide Perovskite Nanocrystals. *J. Am. Chem. Soc.* **2018**, *140*, 2656−2664. (o) Bohn, B. J.; Tong, Y.; Gramlich, M.; Lai, M. L.; Döblinger, M.; Wang, K.; Hoye, R. L. Z.; Müller-Buschbaum, P.; Stranks, S. D.; Urban, A. S.; Polavarapu, L.; Feldmann, J. Boosting Tunable Blue Luminescence of Halide Perovskite Nanoplatelets through Postsynthetic Surface Trap Repair. *Nano Lett.* **2018**, *18*, 5231−5238. (p) Uddin, M. A.; Mobley, J. K.; Masud, A. A.; Liu, T.; Calabro, R. L.; Kim, D.-Y.; Richards, C. I.; Graham, K. R. Mechanistic Exploration of Dodecanethiol-Treated Colloidal $CsPbBr_3$ Nanocrystals with Photoluminescence Quantum Yields Reaching Near 100%. *J. Phys. Chem. C* **2019**, *123*, 18103−18112. (q) Imran, M.; Ijaz, P.; Goldoni, L.; Maggioni, D.; Petralanda, U.; Prato, M.; Almeida, G.; Infante, I.; Manna, L. Simultaneous Cationic and Anionic Ligand Exchange For

DOI: 10.1021/jacs.9b09969
J. Am. Chem. Soc. 2019, 141, 19839−19849

Colloidally Stable $CsPbBr_3$ Nanocrystals. *ACS Energy Lett.* **2019**, *4*, 819−824.
(15) Debuch, H. Über die enzymatische Spaltung des Lecithins aus Sojabohnen. *Hoppe-Seyler's Z. Physiol. Chem.* **1957**, *306*, 279−286
(16) (a) Zhang, X.; Wang, H. C.; Tang, A. C.; Lin, S. Y.; Tong, H. C.; Chen, C. Y.; Lee, Y. C.; Tsai, T. L.; Liu, R. S. Robust and Stable Narrow-Band Green Emitter: An Option for Advanced Wide-Color-Gamut Backlight Display. *Chem. Mater.* **2016**, *28*, 8493−8497. (b) Zhou, Q.; Bai, Z.; Lu, W. G.; Wang, Y.; Zou, B.; Zhong, H. In Situ Fabrication of Halide Perovskite Nanocrystal-Embedded Polymer Composite Films with Enhanced Photoluminescence for Display Backlights. *Adv. Mater.* **2016**, *28*, 9163−9168. (c) Wang, Y.; He, J.; Chen, H.; Chen, J.; Zhu, R.; Ma, P.; Towers, A.; Lin, Y.; Gesquiere, A. J.; Wu, S. T.; Dong, Y. Ultrastable, Highly Luminescent Organic-Inorganic Perovskite-Polymer Composite Films. *Adv. Mater.* **2016**, *28*, 10710−10717. (d) Raja, S. N.; Bekenstein, Y.; Koc, M. A.; Fischer, S.; Zhang, D.; Lin, L.; Ritchie, R. O.; Yang, P.; Alivisatos, A. P. Encapsulation of Perovskite Nanocrystals into Macroscale Polymer Matrices: Enhanced Stability and Polarization. *ACS Appl. Mater. Interfaces* **2016**, *8*, 35523−35533. (e) Meyns, M.; Peralvarez, M.; Heuer-Jungemann, A.; Hertog, W.; Ibanez, M.; Nafria, R.; Genc, A.; Arbiol, J.; Kovalenko, M. V.; Carreras, J.; Cabot, A.; Kanaras, A. G. Polymer-Enhanced Stability of Inorganic Perovskite Nanocrystals and Their Application in Color Conversion LEDs. *ACS Appl. Mater. Interfaces* **2016**, *8*, 19579−19586. (f) Guhrenz, C.; Benad, A.; Ziegler, C.; Haubold, D.; Gaponik, N.; Eychmüller, A. Solid-State Anion Exchange Reactions for Color Tuning of $CsPbX_3$ Perovskite Nanocrystals. *Chem. Mater.* **2016**, *28*, 9033−9040. (g) Huang, H.; Chen, B.; Wang, Z.; Hung, T. F.; Susha, A. S.; Zhong, H.; Rogach, A. L. Water resistant $CsPbX_3$ Nanocrystals Coated with Polyhedral Oligomeric Silsesquioxane and their Use as Solid State Luminophores in All-Perovskite White Light-Emitting Devices. *Chem. Sci.* **2016**, *7*, 5699−5703. (h) Xu, L.; Chen, J.; Song, J.; Li, J.; Xue, J.; Dong, Y.; Cai, B.; Shan, Q.; Han, B.; Zeng, H. Double-Protected All-Inorganic Perovskite Nanocrystals by Crystalline Matrix and Silica for Triple-Modal Anti-Counterfeiting Codes. *ACS Appl. Mater. Interfaces* **2017**, *9*, 26556−26564. (i) Li, Z.; Kong, L.; Huang, S.; Li, L. Highly Luminescent and Ultrastable $CsPbBr_3$ Perovskite Quantum Dots Incorporated into a Silica/Alumina Monolith. *Angew. Chem., Int. Ed.* **2017**, *56*, 8134−8138. (j) Quan, L. N.; Quintero-Bermudez, R.; Voznyy, O.; Walters, G.; Jain, A.; Fan, J. Z.; Zheng, X.; Yang, Z.; Sargent, E. H. Highly Emissive Green Perovskite Nanocrystals in a Solid State Crystalline Matrix. *Adv. Mater.* **2017**, *29*, 1605945−1605951. (k) Gonzalez-Pedro, V.; Veldhuis, S. A.; Begum, R.; Banuls, M. J.; Bruno, A.; Mathews, N.; Mhaisalkar, S.; Maquieira, A. Recovery of Shallow Charge-Trapping Defects in $CsPbX_3$ Nanocrystals through Specific Binding and Encapsulation with AminoFunctionalized Silanes. *ACS Energy Lett.* **2018**, *3*, 1409−1414. (l) Zhou, Y. Y.; Zhao, Y. X. Chemical Stability and Instability of Inorganic Halide Perovskites. *Energy Environ. Sci.* **2019**, *12*, 1495−1511.
(17) (a) Chen, H.; He, J.; Wu, S.-T. Recent Advances on Quantum-Dot-Enhanced Liquid-Crystal Displays. *IEEE J. Sel. Top. Quantum Electron.* **2017**, *23*, 1−11. (b) Ko, Y. H.; Jalalah, M.; Lee, S. J.; Park, J. G. Super Ultra-High Resolution Liquid-Crystal-Display Using Perovskite Quantum-Dot Functional Color-Filters. *Sci. Rep.* **2018**, *8*, 12881−2888. (c) Wei, Y.; Cheng, Z. Y.; Lin, J. An Overview on Enhancing the Stability of Lead Halide Perovskite Quantum Dots and their Applications in Phosphor-Converted LEDs. *Chem. Soc. Rev.* **2019**, *48*, 310−350.
(18) Yin, Y.; Alivisatos, A. P. Colloidal Nanocrystal Synthesis and the Organic-Inorganic Interface. *Nature* **2005**, *437*, 664−670.
(19) (a) De Gennes, P. G. Polymer Solutions near an Interface. 1. Adsorption and Depletion Layers. *Macromolecules* **1981**, *14*, 1637−1644. (b) De Gennes, P. G. Polymers at an Interface. 2. Interaction between two Plates Carrying Adsorbed Polymer Layers. *Macromolecules* **1982**, *15*, 492−500. (c) De Gennes, P. G. Polymers at an Interface: A Simplified View. *Adv. Colloid Interface Sci.* **1987**, *27*, 189−209.
(20) Milner, S. T. Polymer Brushes. *Science* **1991**, *251*, 905−914.
(21) Milner, S. T.; Witten, T. A.; Cates, M. E. Effects of Polydispersity in the End-Grafted Polymer Brush. *Macromolecules* **1989**, *22*, 853−861.
(22) (a) Milner, S. T.; Witten, T. A.; Cates, M. E. A Parabolic Density Profile for Grafted Polymers. *Europhys. Lett.* **1988**, *5*, 413−418. (b) Milner, S. T.; Witten, T. A.; Cates, M. E. Theory of the Grafted Polymer Brush. *Macromolecules* **1988**, *21*, 2610−2619.
(23) (a) Yang, Y.; Qin, H.; Peng, X. Intramolecular Entropy and Size-Dependent Solution Properties of Nanocrystal-Ligands Complexes. *Nano Lett.* **2016**, *16*, 2127−2132. (b) Yang, Y.; Qin, H.; Jiang, M.; Lin, L.; Fu, T.; Dai, X.; Zhang, Z.; Niu, Y.; Cao, H.; Jin, Y.; Zhao, F.; Peng, X. Entropic Ligands for Nanocrystals: From Unexpected Solution Properties to Outstanding Processability. *Nano Lett.* **2016**, *16*, 2133−2138.
(24) (a) Chakrabarti, A.; Nelson, P.; Toral, R. Interpenetrations in Polymer Brushes. *J. Chem. Phys.* **1994**, *100*, 748−749. (b) Israelachvili, J. N. Repulsive "Steric" or "Overlap" Forces between Polymer-Covered Surfaces. *Intramolecular and surface forces*, 3rd ed.; Elsevier, 2011; pp 387−393.
(25) Pang, Z.; Zhang, J.; Cao, W.; Kong, X.; Peng, X. Partitioning Surface Ligands on Nanocrystals for Maximal Solubility. *Nat. Commun.* **2019**, *10*, 2454−2462.
(26) Bertolotti, F.; Protesescu, L.; Kovalenko, M. V.; Yakunin, S.; Cervellino, A.; Billinge, S. J. L.; Terban, M. W.; Pedersen, J. S.; Masciocchi, N.; Guagliardi, A. Coherent Nanotwins and Dynamic Disorder in Cesium Lead Halide Perovskite Nanocrystals. *ACS Nano* **2017**, *11*, 3819−3831.
(27) (a) Murray, C. B.; Norris, D. J.; Bawendi, M. G. Synthesis and characterization of nearly monodisperse CdE (E = sulfur, selenium, tellurium) semiconductor nanocrystallites. *J. Am. Chem. Soc.* **1993**, *115*, 8706−8715. (b) Guzelian, A. A.; Katari, J. E. B.; Kadavanich, A. V.; Banin, U.; Hamad, K.; Juban, E.; Alivisatos, A. P.; Wolters, R. H.; Arnold, C. C.; Heath, J. R. Synthesis of Size-Selected, Surface-Passivated InP Nanocrystals. *J. Phys. Chem.* **1996**, *100*, 7212−7219. (c) Poznyak, S. K.; Osipovich, N. P.; Shavel, A.; Talapin, D. V.; Gao, M.; Eychmüller, A.; Gaponik, N. Size-Dependent Electrochemical Behavior of Thiol-Capped CdTe Nanocrystals in Aqueous Solution. *J. Phys. Chem. B* **2005**, *109*, 1094−1100.
(28) Sercel, P. C.; Lyons, J. L.; Wickramaratne, D.; Vaxenburg, R.; Bernstein, N.; Efros, A. L. Exciton Fine Structure in Perovskite Nanocrystals. *Nano Lett.* **2019**, *19*, 4068−4077.
(29) (a) Park, Y. S.; Guo, S.; Makarov, N. S.; Klimov, V. I. Room Temperature Single-Photon Emission from Individual Perovskite Quantum Dots. *ACS Nano* **2015**, *9*, 10386−10393. (b) Utzat, H.; Shulenberger, K. E.; Achorn, O. B.; Nasilowski, M.; Sinclair, T. S.; Bawendi, M. G. Probing Linewidths and Biexciton Quantum Yields of Single Cesium Lead Halide Nanocrystals in Solution. *Nano Lett.* **2017**, *17*, 6838−6846.
(30) (a) Carney, R. P.; Kim, J. Y.; Qian, H.; Jin, R.; Mehenni, H.; Stellacci, F.; Bakr, O. M. Determination of Nanoparticle Size Distribution Together with Density or Molecular Weight by 2D Analytical Ultracentrifugation. *Nat. Commun.* **2011**, *2*, 335−343. (b) Demeler, B.; Nguyen, T. L.; Gorbet, G. E.; Schirf, V.; Brookes, E. H.; Mulvaney, P.; El-Ballouli, A. O.; Pan, J.; Bakr, O. M.; Demeler, A. K.; Hernandez Uribe, B. I.; Bhattarai, N.; Whetten, R. L. Characterization of size, anisotropy, and density heterogeneity of nanoparticles by sedimentation velocity. *Anal. Chem.* **2014**, *86*, 7688−95. (c) Walter, J.; Gorbet, G.; Akdas, T.; Segets, D.; Demeler, B.; Peukert, W. 2D analysis of polydisperse core-shell nanoparticles using analytical ultracentrifugation. *Analyst* **2017**, *142*, 206−217. (d) Planken, K. L.; Colfen, H. Analytical ultracentrifugation of colloids. *Nanoscale* **2010**, *2*, 1849−69.
(31) Schuck, P. Size-Distribution Analysis of Macromolecules by Sedimentation Velocity Ultracentrifugation and Lamm Equation Modeling. *Biophys. J.* **2000**, *78*, 1606−1619.
(32) (a) Hammersley, A. P.; Svensson, S. O.; Thompson, A.; Graafsma, H.; Kvick, Å.; Moy, J. P. Calibration and Correction of Distortions in Two-Dimensional Detector Systems. *Rev. Sci. Instrum.* **1995**, *66*, 2729−2733. (b) Glatter, O. Determination of Particle-size Distribution Functions from Small-Angle Scattering Data by means of the Indirect Transformation Method. *J. Appl. Crystallogr.* **1980**, *13*, 7−11.

DOI: 10.1021/jacs.9b09969
J. Am. Chem. Soc. 2019, 141, 19839−19849

(33) (a) Burian, M.; Fritz-Popovski, G.; He, M.; Kovalenko, M. V.; Paris, O.; Lechner, R. T. Considerations on the Model-Free Shape Retrieval of Inorganic Nanocrystals from Small-Angle Scattering Data. *J. Appl. Crystallogr.* **2015**, *48*, 857−868. (b) Burian, M.; Amenitsch, H. Dummy-atom modelling of stacked and helical nanostructures from solution scattering data. *IUCrJ* **2018**, *5*, 390−401.

(34) (a) Kim, H.-S.; Lee, C.-R.; Im, J.-H.; Lee, K.-B.; Moehl, T.; Marchioro, A.; Moon, S.-J.; Humphry-Baker, R.; Yum, J.-H.; Moser, J. E.; Grätzel, M.; Park, N.-G. Lead Iodide Perovskite Sensitized All-Solid-State Submicron Thin Film Mesoscopic Solar Cell with Efficiency Exceeding 9%. *Sci. Rep.* **2012**, *2*, 591. (b) Im, J. H.; Lee, C. R.; Lee, J. W.; Park, S. W.; Park, N. G. 6.5% efficient perovskite quantum-dot-sensitized solar cell. *Nanoscale* **2011**, *3*, 4088−4093.

(35) Mooney, M. The Viscosity of a Concentrated Suspension of Spherical Particles. *J. Colloid Sci.* **1951**, *6*, 162−170.

(36) Yuan, G.; Ritchie, C.; Ritter, M.; Murphy, S.; Gómez, D. E.; Mulvaney, P. The Degradation and Blinking of Single $CsPbI_3$ Perovskite Quantum Dots. *J. Phys. Chem. C* **2018**, *122*, 13407−13415.

DOI: 10.1021/jacs.9b09969
J. Am. Chem. Soc. 2019, 141, 19839−19849